Orbital
The electronic journal of chemistry

the electronic journal of chemistry

Full Paper | http://dx.doi.org/10.17807/orbital.v17i4.22921

Computational Methods as Screening Toll for Triazole Natural Products Derivatives as Potential β-Tubulin Inhibitors for *Fusarium graminearum*

Larissa de Souza Gasques* [a], Pedro Alves Bezerra Morais [a], Arlan da Silva Gonçalves* [b], and Heberth de Paula* [c]

Phytopathogenic fungi like *Fusarium graminearum* are the cause of the disease gibberellosis, also known as Fusarium head blight (FHB). This disease shows significant losses in agriculture and effects on global economy. Nevertheless, this condition can be reduced with the use of commercial fungicides. Thus, this work describes computational studies performed on a group of natural products triazole derivatives using as starting point a small library of quinazolines synthesized by the literature. These quinazolines were applied to build QSAR models. Furthermore, using the Swiss Model server, a comparative modelling of the β-tubulin protein was realized to test the models and the compound 15, a triazole derivative of thymol successfully was further through both the QEPest and ProTox II toxicity tests. The behavior and stability between compound 15 and β-tubulin were then evaluated by 200 ns of molecular dynamics in comparison to carbendazim as standard inhibitor. Finally, the compound 15 revealed a stable complex with the protein throughout the simulation, exhibiting low fluctuations in the RMSF, indicating good interactions with the residues present. The investigation of the free energy of binding supports this, showing that whereas carbendazim had an MM/GBSA of -18 kcal/mol, thymol-derived 15 had an MM/GBSA of -44 kcal/mol.

Graphical abstract

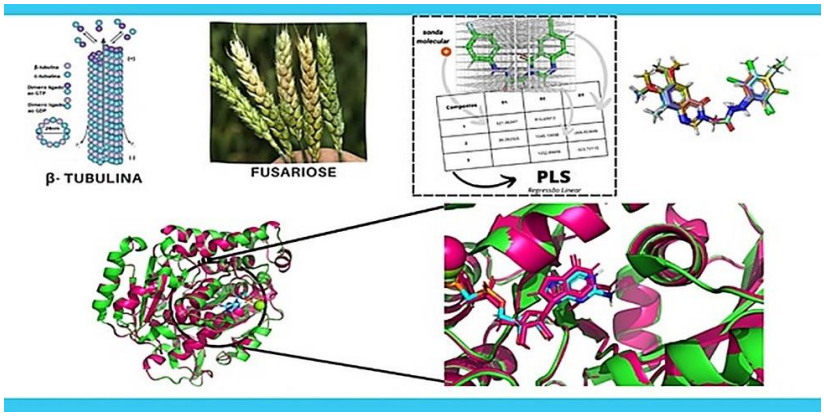

Keywords

β-tubulin
Carbendazim
Fusarium graminearum
Molecular Dynamics
QSAR

Article history

Received 27 Feb 2025
Accepted 04 Jun 2025
Available online 17 Aug 2025

Handling Editor: Marcos S. Amaral

[a] Postgraduate Program in Agrochemistry - Center for Exact, Natural and Health Sciences in Institution Federal University of Espírito Santo (UFES) - Alto Universitario, S/N - Guararema, Alegre - ES, 29500-000, Brazil. [b] Department of Chemistry in Institution Federal University (UFES) and Federal Institute of Education, Science and Technology of Espírito Santo (IFES), Av. Fernando Ferrari, 514 - Goiabeiras, Vitória - ES, 29075-910 and Av. Min. Salgado Filho, 1000 - Soteco, Vila Velha - ES, 29106-010, Brazil. [c] Department of Pharmacy and Nutrition in Institution Federal University of Espírito Santo (UFES) - Alto Universitario, S/N - Guararema, Alegre - ES, 29500-000, Brazil.*Corresponding author. E-mail: **lwgasques@gmail.com**

1. Introduction

Currently, one of the most significant crops in agriculture is the wheat (*Triticum spp*.), that provides food and nutrition for both humans and animals [1]. *Fusarium graminearum* is the causative agent of gibberellosis and is also known as Fusarium head blight (FHB). This fungus affects mainly cereals such as wheat, corn, oats, and barley. Losses are demonstrated by lower grain quality and crop production, as well as the presence of mycotoxins in the grain [2], that causes billion of dollars in losses annually [3] and are harmful to animal and human health [4].

The disease can be observed at the spike stage of the plant and particularly during the flowering stage, which can last until the grain starts to ripen. A pink clump of spores that forms on the spikelet and is readily seen in the field is indicative of symptoms [5]. Alternatively, as a result of the pathogen's internal growth and subsequent propagation inside the spike, the spikelets may blanch prematurely. Furthermore, the grains become wrinkly, shriveled, and variably colored when the fungus settles on them, impairing their ability to mature [6]. Since the early 1970s, Fusarium has been extensively controlled with benzimidazole fungicides [7]. The most often utilized member of the benzimidazole chemical group is methyl-2-benzimidazole carbamate, also known as carbendazim.

Natural fungicidal products are emphasized, with a focus on the idea of "sustainable agriculture" and their role in lowering fungal infections in the agricultural ecosystem. They serve as effective tools for combating various issues related to infections, pathogenesis, and disease protection [8]. Besides, there is a growing trend in incorporating natural products into inhibitor discovery programs [9]. Althought, natural products can target tubulin as inhibitor or promoter the microtubule's polymerization [10]. Additionally, they have the ability to interfere with the synthesis of tubulin, which can stop mitosis, induce apoptosis, and prevent microtubule assembly [11].

Synthetic fungicides target the β-tubulin protein by preventing the construction of α and β heterodimers, which are essential for biological functions such as cell motility, division, and signaling [12]. The fungus dies as a result of the inhibition of microtubule production, which creates multinucleated cells that are unable to divide. Carbendazim has been used so frequently that it is now a recurring contaminant in both soil and water. According to previous studies, the imidazole ring significantly combines fungicide residues and metabolites into the organic matter of the soil, allowing the fungicide to persist in the environment [13].

New techniques were developed to produce substances that are less damage to the environment in an effort to mitigate these effects. To aid in the development of novel agrochemical candidates with strong antifungal potential, computational techniques such as Quantitative Structure-Activity Relationship (QSAR) analysis are used to provide crucial information on the relationship between chemical structure and biological activity from a substance. This method greatly lowers operational expenses by simplifying the process of finding new bioactive chemical [14]. Consequently, minor modifications to the molecule's structure can instantly affect its bioactivity, which makes this technique essential for optimizing chemical items that have not been tested before [15]. So, we used a group of 27 quinazoline derivatives described and analysed their biological activity against *F. graminearum* by Wang and coworkers [16] to constructed the models of QSAR-2D and 3-D.

Molecular dynamic simulation and docking molecular are two more essential in silico ways to analyze the behavior of a protein and its ligand. Although each has its unique characteristics, both are typically utilized to comprehend the complex, its interactions, and their binding affinity. After the methods for treating FHB illness were identified, we suggested screening natural product-derived triazoles found in the literature [17-19] to determine their potential as β-tubulin inhibitors against *Fusarium graminearum*.

2. Results and Discussion

QSAR-2D MODELS

The computation of molecular descriptors is required when building models. Therefore, the PaDEL program was used to describe the compounds and provide a numerical representation of their properties. Descriptors with high correlation were eliminated. The 19 compounds that were separated to create the QSAR models during the process of division training (70%) and testing (30%) using the k-medoid GUI v1.1 software were the compounds that were used to develop the models. As stated in the approach above, eight compounds that were separated during the test were used for validation.

Using Best Subset Selection software, descriptors whose model yielded a q^2 above 0.6 and had the strongest association with biological activity were found. After that, the data were further processed with the Jamovi program (2022), allowing for the creation of a statistically meaningful model. The topological descriptors JGI1 and VE3_D in **Table 1** represent the best model; the remaining descriptors are included in annex I in the supplementary material.

For external validation, the antifungal activity of the test set was predicted using equation 1. The difference between the experimental and predicted pEC_{50s} was used to compute the residuals. Since Model 4 had the highest r^2_{test} = 0.764 produced the best predicted correlation coefficient, it was the best. See the additional material, annex I for viewing the other models. Notably, the model's predictive capacity increases as the predicted correlation coefficient (r^2_{test}) becoming closer to 1. This approach is relevant to the external validation of the models using the test set. In statistical modeling, a model is desired to be able to explain a significant portion of the variability in the test data, as shown by an R^2 close to 1.

The generated model can be visualized by the following linear combination:

$$pEC_{50} = 5.43 + 23.87 * JGI1 + 1.33 * VE3\_D \quad \text{(Eq. 1)}$$

Table 1. Statistical outcomes of the best model found using QSAR-2D as determined by Jamovi software.

QSAR-2D								
Model	**Descriptors present**	**R^2**	**R^2 adjusted**	**Durbin-Watson**	**VIF**	**Shapiro–Wilk**	**q^2**	**r^2_{test}**
4	JGI1 - VE3_D	0.797	0.771	1.46	1	0.491	0.743	0.764

CoMFA MODEL

Table 2 displays the best model validation findings for each type of partial atomic charge, where the models were fitted at several theoretical levels: ab initio (HF 3-21G and HF 6-311G), semiempirical (PM7, RM1, AM1-BCC), empirical (Gasteiger, Gasteiger-Hückel, and MMFF94), and DFT (B3LYP/6-311G). The annex II of supplementary material contains the outcomes of every focus model.

The loads determined by the AM1-BCC method produced better results, with lower prediction error (SEP = 0.134) in the leave-one-out method and subsequently greater q^2 (0.980) among the findings produced by the internal validation of the training set of molecules (19). However, cross-validation (q^2) alone is not enough to validate the model because, according to Leemans *et al*. [48], for the prediction to be reliable, it needs to be validated using the molecules in the test set. The external validation performed by the test set will inform the predicted r^2, which must be above 0.5 [49].

Consequently, all of the models underwent external validation, producing an r^2_{test} for each of the eight test molecules loaded with various partial atomic charge types to determine the predicted biological activity. Among the models presented, the one with the best predictive capacity was the restricted electrostatic potential (RESP) charge model using the HF 6-311G method, which obtained the highest predicted correlation coefficient (r^2_{test} = 0.834).

Madhavan *et al*. [28] reported that, compared with empirical or semiempirical models, QSAR models with more complex partial atomic charge calculations, such as HF and DFT calculations, exhibited a stronger correlation with biological activity. This partially corroborates the findings of this work since the semiempirical PM7 method outperformed the DFT method in terms of outcomes. Therefore, as CoMFA is a comparative molecular field analysis technique that focuses on steric and electrostatic fields, the PM7-derived charges more adequately captured the effects relevant to this analysis.

CoMSIA MODEL

Three additional descriptors, hydrophobic, donor, and hydrogen bond acceptor, that are absent from CoMFA are used in the CoMSIA method [15]. The descriptors that most significantly influenced the type of partial atomic charge that was estimated are included in **Table 3**. It is evident that the most prominent characteristics for this training set are hydrophobic and electrostatic. The model was not improved by adding additional parameters. The annex III of supplementary material contains the outcomes of every focus model.

Table 2. The statistical characteristics that correspond to the QSAR-3D CoMFA models that were developed based on partial atomic charge calculations. Model regression coefficient (W) and focus (D).

	Statistical parameters PLS - CoMFA								
Charge Methods	**q^2**	**SEP**	**r^2**	**SEE**	**N**	**r^2_{test}**	**S**	**E**	**Focus**
PM7	0.946	0.217	0.997	0.05	6	0.664	0.412	0.588	W0.7D1.0
RM1	0.941	0.227	0.997	0.054	6	0.008	0.466	0.534	W0.7D1.0
Gasteiger-Marsili	0.909	0.251	0.956	0.176	3	0.181	0.534	0.466	W0.7D1.0
Gasteiger-Hückel	0.894	0.272	0.961	0.165	3	0.296	0.540	0.460	W0.7D1.0
MMFF94	0.902	0.280	0.994	0.068	5	0.413	0.406	0.594	W0.7D1.0
AM1-BCC	0.980	0.134	0.997	0.048	6	0.476	0.384	0.616	W0.7D1.0
HF 3-21G	0.841	0.332	0.950	0.187	3	0.316	0.505	0.495	W0.7D1.0
HF 6-311G	0.826	0.348	0.959	0.169	3	0.809	0.479	0.521	W0.7D1.0
DFT 6-311G	0.569	0.531	0.855	0.307	2	0.659	0.439	0.561	W0.3D1.0
RESP HF 6-311G	0.834	0.340	0.958	0.171	3	**0.834**	0.481	0.519	W0.7D1.0

For internal validation, the following equation was used: q^2_{LOO} - cross-validation coefficient calculated using the "leave one-out" method; SEP - standard error of prediction; N: number of components; r^2 - correlation coefficient; and SEE - standard error of estimate. For external validation, the r^2_{test} was used to predict the correlation coefficient. Fractions: S: Steric; E: Electrostatic.

Table 3. The statistical characteristics that correspond to the QSAR-3D CoMSIA models that were developed based on partial atomic charge calculations. Model regression coefficient (W) and focus (D).

	Statistical parameters PLS - CoMSIA											
Charge Methods	**Focus**	**q^2**	**SEP**	**r^2**	**SEE**	**N**	**r^2_{test}**	**A**	**E**	**S**	**H**	**D**
PM7	W0.7D1.5	0.941	0.21	0.986	0.103	4	0.542		0.461	-	0.403	0.135
RM1	W0.7D1.0	0.974	0.14	0.985	0.105	4	0.784		0.564	-	0.436	-
AM1-BCC	W0.7D1.0	0.95	0.209	0.991	0.088	6	0.644	0.059	0.533	-	0.355	0.053
Gasteiger-Marsili	**W0.9D1.5**	**0.956**	**0.195**	**0.987**	**0.106**	**6**	**0.858**	-	0.415	-	0.585	-
Gasteiger-Hückel	W0.9D1.5	0.931	0.219	0.973	0.137	3	0.816	-	0.381	-	0.619	-
MMFF94	W0.9D1.5	0.94	0.205	0.974	0.134	3	0.728	0.072	0.446	-	0.482	-
HF 3-21G	W0.9D1.5	0.865	0.343	0.972	0.157	6	0.791	-	0.648	-	0.352	-
HF 6-311G	W0.9D1.5	0.749	0.418	0.927	0.226	3	0.803	-	0.636	-	0.364	-
DFT 6-311G	W0.9D1.0	0.915	0.272	0.910	0.242	2	0.601	-	0.561	-	0.439	-
RESP HF 6-311G	**W0.9D1.0**	**0.780**	**0.392**	**0.924**	**0.229**	3	**0.857**	-	0.511	-	0.489	-

For internal validation, the following equation was used: q^2_{LOO} - cross-validation coefficient calculated using the "leave one-out" method; SEP - standard error of prediction; N: number of components; r^2 - correlation coefficient; and SEE - standard error of estimate. For external validation, the r^2_{test} was used to predict the correlation coefficient. Fractions: S: Steric; E: Electrostatic.

Compared to all other methods, the CoMSIA model's predictive ability utilizing the Gasteiger–Marsili method (r^2_{test} = 0.858) was the most accurate; the CoMSIA model was constructed with only electrostatic (E) and hydrophobic (H) descriptors. Despite the similarity to the model calculated with the RESP HF 6-311G charges, whose predicted r^2_{test} was 0.857 in the external validation, it did not have a higher q^2_{LOO} than the Gasteiger–Marsili model.

The CoMFA and CoMSIA models both satisfy the requirements that a $q^2_{LOO} > 0.5$ and a $r^2 \geq 0.5$ be established to achieve accuracy in estimating biological activity. Thus, according to Kumar and coworkers [50], who determined that descriptors are critical for linking observed activity, all the PLS models that were generated were statistically significant. Moreover, the outcomes of the external validation indicated that the created model has outstanding accuracy.

A scatter plot was created with all of the training (orange) and test (blue) compounds for improved visibility, as shown in **Graph 1**.

The results below yield the r^2_{test}, which was 0.764 for QSAR-2D, 0.834 for CoMFA, and 0.858 for CoMSIA. The results of the external validation suggest that the models generated had excellent accuracy.

The kind of partial atomic charge that is employed directly affects the precision of QSAR models. As noted by Kumar *et al*. [50] the estimation of these charges yields a higher cross-validation coefficient (q^2_{LOO}) and computes the molecular interaction fields (MIFs), which in turn explains the variance of chemical structures with respect to their biological activity. In addition to q^2, the correlation coefficient (r^2) is an important parameter for assessing the quality of PLS analysis, where it indicates predictive ability and self-consistency [51].

Graphic 1. Correlations of the experimental and predicted pEC_{50} values for the training (orange) and test (blue) sets.

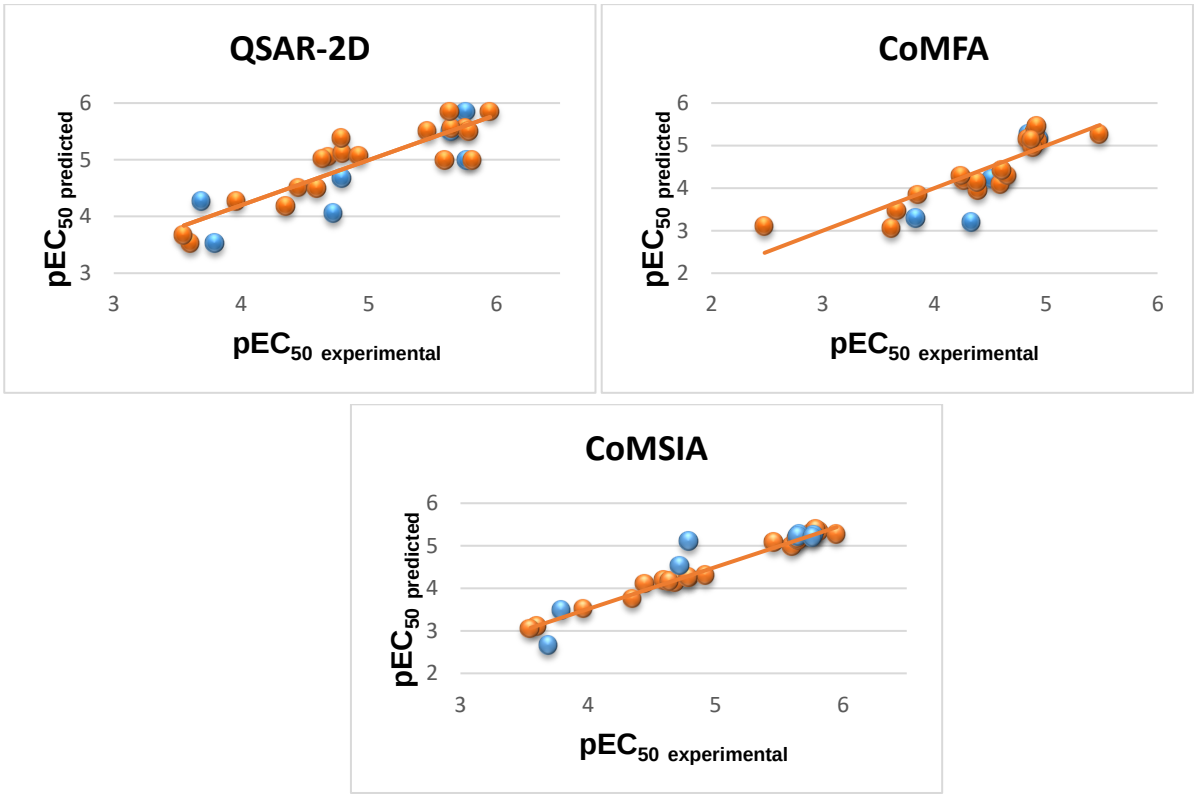

Contour maps

Contour maps serve as useful tools for identifying regions where chemical changes may impact biological activity. It has the ability to highlight the areas in which any modifications in the elements will have an influence on the steric, electrostatic, and hydrophobic characteristics as well as the ability to donate and accept hydrogen bonds, which may result in alteration of the biological property in question [51].

The polyhedra on the maps are colored; those in yellow and green indicate the locations that are favorable or unfavorable for bulky groups (steric factors), respectively. The regions represented by red and blue polyhedra indicate the regions in which the electronegative groups are unfavorable or favorable for fungicidal activity, respectively. These regions should be emphasized because they can be utilized to change structures and create novel compounds [15]. The contour maps were created using the training set's highest active chemical (**25**).

The contour map with steric effects from the comparative molecular field analysis (CoMFA) is shown in **Figure 1**. The presence of bulky aromatic groups is likely the reason why the yellow regions are considered unfavorable regions. This is evident from the fact that the pEC_{50} value of compounds containing bulky groups in this area was lower. A large yellow contour placed on the benzene ring indicates that larger substituents are not preferred in this region, as Krishna *et al*. [51] noted in their steric effect map. According to Walter, Almeida, and Nunes [52], a yellow surface indicates that smaller ligands promote steric interactions, increasing the biological activity of the examined molecule. Therefore, the most active compound (**25**) in this study has only one chlorine atom in the yellow region.

The contour map incorporating the electrostatic effect shows that the addition of electronegative elements is likely beneficial and can increase the predicted activity, as indicated by the blue polyhedra (SYBYL-X, 2013). When added at the end, substituents that increase the negative electrostatic potential should boost activity, which is regulated by the blue region of the molecule [52]. Consequently, as illustrated in **Figure 1**, the most active chemical (**25**) in this map has highly electronegative nitrogen and oxygen atoms within its structure, yet these are encircled by the blue zone. Conversely, red polyhedra represent areas where positive charges are advantageous; in these locations, negatively charged atoms

render the molecule unsuitable for biological activity. In contrast, the lone fluorine atom in the set of training molecules is located in the red polyhedron, an area that is unfriendly to electronegative groups. Despite this, the compound remained the most active of all the others.

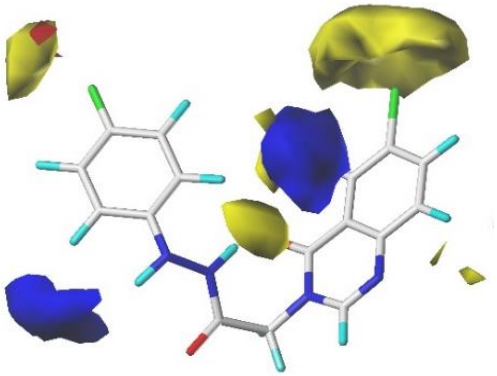

Fig. 1. CoMFA contour map of the most active compound (25), with the RESP charge HF6-311G at a focus W0.7D1.0. Sterically disadvantaged areas are shown in yellow polyhedra. Electrostatically favored areas are shown in blue polyhedra. Source: Images taken from Sybyl-X.

Figure 2 displays the CoMSIA contour map, which was created using the Gasteiger–Marsili model; the descriptors used were hydrophobic (58.5%) and electrostatic (41.5%). El-Mernissi *et al*. [53] also noted these two interactions and concluded that they were important for enhancing inhibitory activity. Based on these two descriptors, they created four novel tubulin protein inhibitors.

The presence of hydrophilic groups in the magenta region tends to increase biological activity, since this region are unfavorable for the hydrophobic action of the most active molecule (**25**). This area of the molecule is unfavorable for the inclusion of benzene rings or apolar groups, and the addition of more apolar groups often reduces biological activity. In support of this idea, substitutions of hydrophilic groups such as hydroxyl groups increase biological activity, according to Nilewar and Kathiravan [54]. Since the hydrophobic area is unfavorable, Ashraf and colleagues [55] also verified that activity increases when this region is replaced by hydrophilic molecules.

The region shown in blue is advantageous for the substituent there, which in this case is fluorine, with reference to the electrostatic action on CoMSIA. This area favors the presence of electronegative atoms, which increases the biological activity of this element.

The least active molecule (**8** with pEC_{50} = 3.0488) only has substituents on R_2 (2 Cl), whereas the most active molecule (**25** with pEC_{50} = 5.4505) has substituents on R_1 (Cl) and R_2 (F). Compound **25** has a chlorine at the -to position (R_1), but compound **8** does not have any substituents on the quinazoline ring. This difference in ring structure can be used to explain why compound **25** has a greater electrostatic potential than compound **8**. The compound's activity is increased by substitution by electron-donating groups, as shown by the blue contour in the R_2 area. Ashraf and coworkers [55] support this observation.

Therefore, fluorine is more effective than two chlorine atoms, which is what happens with the compound with the lowest biological activity. Since fluorine is more electronegative than chlorine, this explains the difference in antifungal activity between these two compounds.

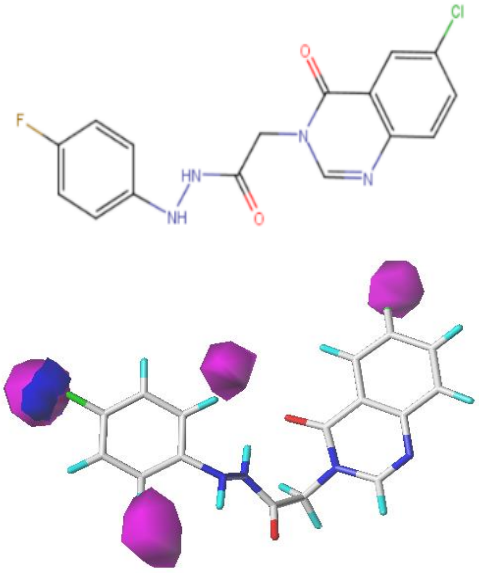

Fig. 2. CoMSIA contour map of the most active compound (25), with Gasteiger-Marsili charge at focus W0.9D1.5. The electrostatically favored area is shown in the blue polyhedron. The nonfavored hydrophobic areas are shown in magenta polyhedral.

TRIAZOLE-DERIVATIVE NATURAL PRODUCTS SCREENING

Triazole derivatives are widely utilized globally and are strategically evaluated due to their ability to reach a broad range of species, for example, through foliar spraying on growing crops such as cereals and horticulture or through seed treatment [56]. Since the 1970s, triazole fungicides have been widely employed in agriculture to protect plants due to their high chemical stability and low biodegradability [57]. The biological activity predictions for every molecule in our library group are shown in **Table S25** on Annex VI of the supplemental material, which is the result of the QSAR-2D and -3D models' development and analysis. Nevertheless, following model testing, **Figure 3** displays the top candidates with the highest biological activity.

Therefore, in terms of QSAR-2D, the best compounds are **21** and **25**, from isatin, towards of to the 32 molecules from the compound library employed in this in silico experiment. CoMFA evaluates thymol (**15**) and isatin derivatives (**20**), and only isatin derivatives (**22**, **27**) are evaluated by CoMSIA.

BEST CANDIDATE COMPOUNDS

Contour maps are useful for the creation of new drugs because they make it possible to determine whether a substitute will be advantageous for increasing biological activity. The library of compounds (triazole derivatives) was superimposed using the CoMFA and CoMSIA contour maps of the most active compound (**25**), as previously mentioned (see **Figure 4**).

It is evident that various colors were used to highlight the molecules in the compound library to distinguish the most active molecule (**25**), which is shown in light blue. The six best triazoles have tiny groups at the right end, as shown by examining the steric fields. The positions in which the triazoles were oriented in the correct directions according to

the contour maps were chosen for docking-based alignment at the crystallographic ligand site. As previously stated, yellow polyhedra represent areas where only little ligands enhance biological activity. Therefore, of the hundred conformations that each triazole obtained during molecular docking, only those containing smaller branches facing the ring of the crystallographic ligand itself were selected.

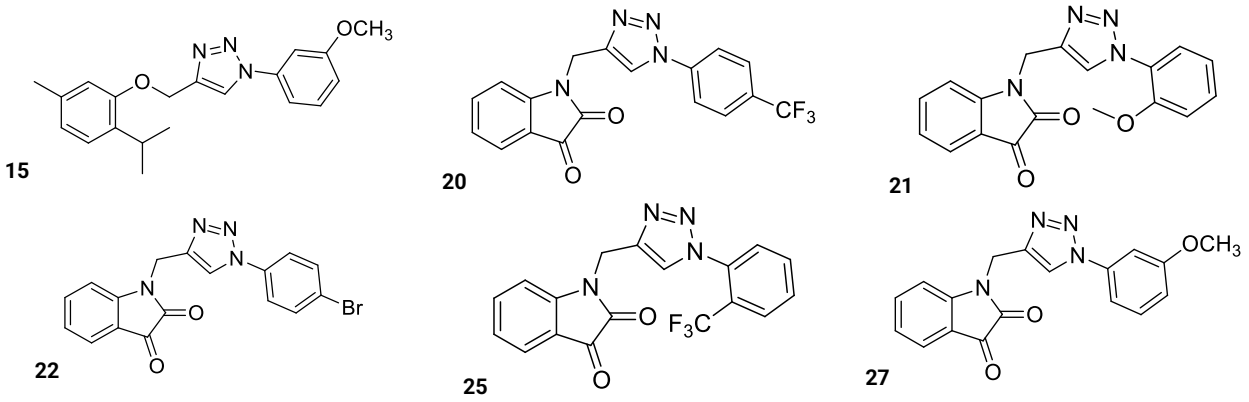

Fig. 3. Structures of the compounds with the best biological activity predicted by the 2D and 3D QSAR models (CoMFA and CoMSIA).

It is well known that apolar regions negatively impact biological activity in the hydrophobic zones found in the CoMSIA contour map. Consequently, the presence of hydrophilic components in the magenta zone enhances their interaction. Regarding this, hydrophilic substituents are present on the right side of triazoles compounds, in the same area where a magenta polyhedron can be found in the CoMSIA contour map. Furthermore, the triazoles **22** and **27** contributed more to the higher antifungal activity than the more active molecule (**25**) derived from quinazoline, which was utilized to build the QSAR models.

Concerning the electrostatic field, it is well known that biological activity tends to increase in the blue zone where there are more electronegative atoms. Nitrogen and oxygen were thus found in the contour map region, which was advantageous for accessing these substituents on the triazoles, which were determined to be the best candidates. Compared to compound **25**, which has the highest pEC_{50} among the others, the compound generated from isatin **22** was more active in the model. It is evident that the components, which are parallel to one another in both compounds and have identical chain sizes, are similarly positioned and aligned.

The most active compound (**25**) had an actual experimental biological activity of 5.450 $mol.L^{-1}$ for the fungus *F. graminearum*, whereas its predicted activity (pEC_{50}), as determined by CoMSIA in the best model constructed, was 5.363 $mol.L^{-1}$. The more active compound was outperformed in this regard by isatin-derived compounds **22** and **27**, with **22** having a pEC_{50} = 5.539 $mol.L^{-1}$ and **27** having a pEC_{50} = 5.509 $mol.L^{-1}$.

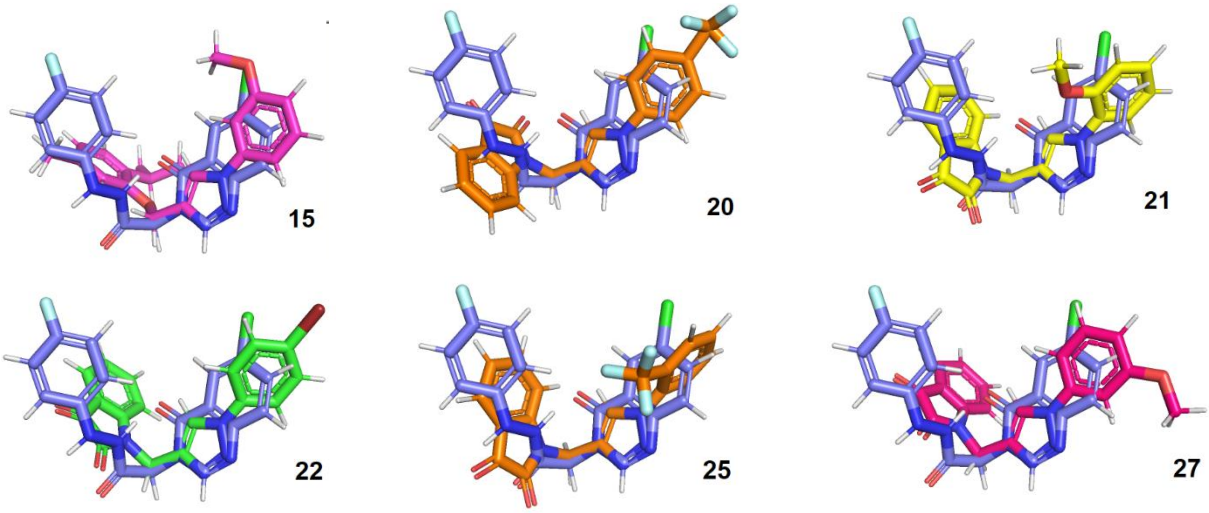

Fig. 4. Overlay of the triazole compounds with the most active compound (25) (light blue color) from the training set of QSAR models.

As can be observed, the compound library was able to predict a higher antifungal activity than the quinazoline-derived compound **25** in the model, although it was still unable to outperform the commercial fungicide carbendazim's experimentally estimated activity (5.638 $mol.L^{-1}$).

COMPARATIVE MODELING

Since strong ligand-target receptor binding is necessary for activity, studying the molecular structure of the β-tubulin protein is crucial for comprehending the mechanism of action of carbendazim [58].

The NCBI database was utilized to obtain the main sequence of the β-tubulin protein from the fungus *Fusarium graminearum*, which the fasta code for this sequence was Q4HZS8.1. Comparative modeling was performed using the crystallographic structure of β-tubulin from the microtubule complex of *Homo sapiens* (PDB: 7ZCW), which was also used by Ramirez-Rios and associates [59], utilizing the Swiss Model server (swissmodel.expasy.org/workspace/) [60].

A validation of the suggested model revealed GMQE (Global Model Quality Estimate) values of 0.87 and QSQE (Quaternary Structure Quality Estimate) values of 0.40; the optimal values are above 0.7 [61]. The selected template was 7ZCW.1. G, which had 82.70% sequence identity. During the modeling process, these values offer quality estimates. At the tertiary and quaternary structure levels, GMQE and QSQE provide the expected estimates of the final model, enabling the identification of the best models [60].

A Qualitative Model Energy Analysis (QMEAN) of 0.84 ± 0.5 was the result of the Swiss Model's validation of the model. The primary geometric features of the protein structures were described by the scoring function (QMEAN), which indicates that models with a quality score of 0.5 are of good quality [62].

Bindewald and Skolnick [63] revealed that a protein extracted from the PDB should have a resolution of less than 3 Å to enhance the focus on that interaction space and support accurate atom visualization. Following comparative modeling, the 7ZCW protein was suggested as a model, and it has a resolution of 3.60 Å. However, the validation of the comparative modeling carried out by the PROCHECK and VERIFY3D platforms (https://saves.mbi.ucla.edu/) showed a quality and efficient model, where VERIFY3D observed 84.98% of the residues with an average equal to or greater than 0.1. The Ramachandran graph analysis results demonstrate that the model's quality is good, with 91.4% of the torsional angles falling inside the advantageous zone. An effective model of acceptable quality must contain values above 90% of the residues in favorable regions. This conformation provides crucial information for selecting an effective model that does not contain steric hindrance in the side chains of amino acids [64]. In this regard, we concluded that the predicted protein was validated with PROCHECK.

Since the modeled protein had no ligand, the template PDB (7ZCW) was used, and all the chains (A, B, C, D, E, F, G, H) were downloaded. According to the PDBSum platform (http://www.ebi.ac.uk/thornton-srv/databases/pdbsum/), chains A and E are identical, as are B= F= G= H and C and D. To reverse the situation of the template protein (7ZCW.1. G) without a ligand, the original ligands were inserted manually. This procedure was checked in PyMOL, where an alignment between the two proteins verified their overlap (RMSD = 0.208 Å) and confirmed that the crystallographic ligand was in the same location as the 7ZCW protein. **Figure 5** shows the PyMOL alignment of the template and the modeled protein.

Leucine (L) is located at position 240 of β1-tubulins in the majority of phytopathogenic fungi, and this was confirmed in this work using comparative modeling. Nevertheless, studies have shown that some wild fungi in this same location also contain phenylalanine (F) and that resistance to benzimidazole fungicides is caused by this modification [65]. These data suggest that the protein that was constructed may actually be fungicide sensitive rather than resistant.

DOCKING MOLECULAR

Redocking the ligand

The coordinates of the crystallographic ligand of the PDB: 7ZCW protein were found using the redocking methodology in the four scoring functions of Gold 2022.3.0 software (https://www.ccdc.cam.ac.uk/solutions/software/gold/) - GoldScore, ASP, ChemPLP and ChemScore. There are two crystallographic ligands in this protein. The binding site between the α and β chains of the tubulin protein is the guanosine triphosphate (GTP) ligand, which interacts more with the α chain and only one amino acid (Lys252) from the β chain. Furthermore, only the β chain is connected to the second ligand, G2P (guanylate ester of phosphomethylphosphonic acid). Redocking was performed on top of the G2P ligand since the protein that was modeled following alignment with the model protein was more similar to it, as illustrates in Annex VIII on supporting information. The overlap of both ligands is also there.

When the RMSD (Root Means Square Deviation) is less than 2 Å, the approach is deemed acceptable and efficient since it establishes the best fitting position between the ligand and the protein [66]. In simple terms, it evaluates how well and accurately the predicted ligand positions match the real (or crystallographic) positions of the ligands when they bind to the target protein.

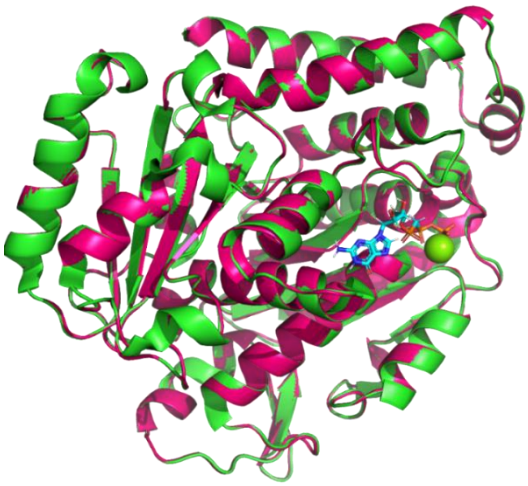

Fig. 5. Protein model (in pink, 7ZCW.1. G) by Swiss Model using the protein template (green: PDB: 7ZCW). Alignment with an RMSD of 0.208 Å.

Molecular Dynamics Simulation and frame extraction

After the molecular dynamics was completed, the complex under study had a collection of different conformations known as frames, totaling 5000 frames throughout the course of the 100 ns journey. For comparative purposes, the ligand and protein's RMSD over time were initially determined before delving into the analysis of the individual frames obtained from the molecular dynamics trajectory. The 50 best frames were chosen after a cutoff was reached, with the lowest RMSD values serving as the selection criterion. The supplemental material contains the commands that are utilized.

Ensemble docking

By examining several protein conformations (extracted from frames generated by molecular dynamics), it was possible to find a range of potential interactions between the protein and the ligand. This approach allowed for a more

extensive investigation made feasible by the application of ensemble docking.

The fifty frames with the lowest root mean square deviation (RMSD) values were selected for redocking using the Gold 2022.3.0 program via the same previously standardized ASP 7 Å score function. The selected cluster in the '.pdb' file was then separated from its ligand with PyMOL 2.5.2 software. The protein was prepared by adding the hydrogens, and the ligand had its -3 formal charge added by MOPAC using the PM7 semiempirical method.

The cluster 700 was chosen to perform molecular docking of the triazole derivatives, since the new RMSD was 0,5779 Å instead of 1,0851 Å before the ensemble docking. The table S25 of supporting information show all clusters during this step.

Intermolecular interactions

The interactions between the amino acids from protein cluster 700 according to the ASP 7Å function are depicted in **Figure 6**. According to Discovery Studio Visualizer, the hydrogen bonds are shown in dark green, the weak van der Waals contacts are shown in light green, and the ionic interactions with magnesium (Mg^{2+}) are shown in orange.

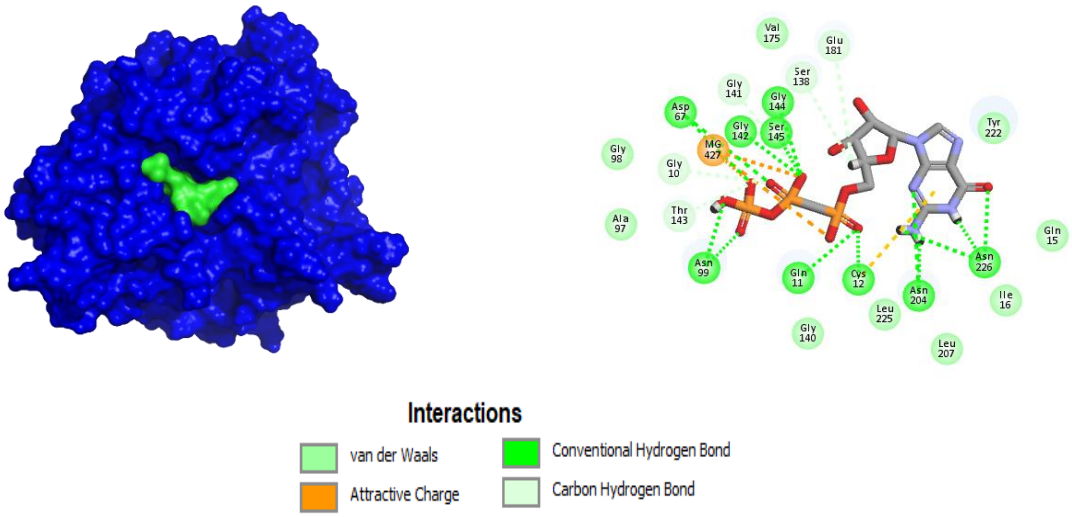

Fig. 6. Interactions between the G2P ligand and the amino acids present in the β-tubulin protein, derived from the cluster with the lowest RMSD, selected after molecular dynamics.

To identify the interaction of the fungicide with the protein's active site, carbendazim was downloaded from PubChem (ID: 25429) and optimized with a mülliken charge using the PM7 method. When its protonation level in the Marvin Sketch was examined, it was found to have zero total charge. Next, the binding affinity of carbendazim was predicted using molecular docking. In addition, the best candidates from the library of compounds that obtained the best antifungal activity results were analyzed using QSAR models, as shown in **Table 4**.

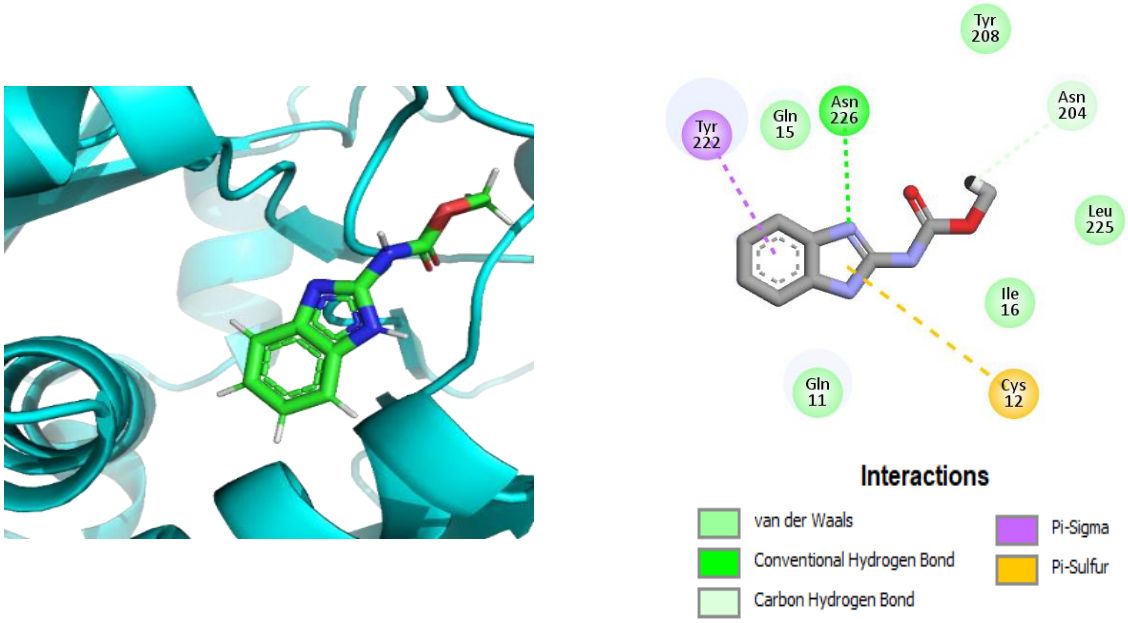

Fig. 7. Interactions between carbendazim and the modeled protein β-tubulin (7ZCW.1. G), after molecular docking. The carbendazim-protein complex was extracted from the Gold software with the solution that obtained the highest score for the ASP 7 Å function.

Table 4. List of the amino acids that interact with the crystallographic ligand of the β-tubulin protein (7ZCW), which were also detected in the compound library after prediction of the antifungal activity of the QSAR models.

Ligand Cristal	15	20	21	22	25	27	CBZ
Asn204	x	x	x	x	x	x	x
Asn226	x	x	x	x	x	x	x
Cys12	x	x	x	x	x	x	x
Gln11	x	x	x	x	x	x	x
Asn99	-	x	x	x	x	x	-
Asp67	-	x	x	-	x	x	-
Gly142	-	x	x	x	x	x	-
Ser145	-	x		-	x	x	-
Gly144	-	x	x	x	x	x	-
Gly10	-	x	x	-	x	x	-
Thr143	-	x		x	x	x	-
Gly141	-	x	x	x	x	x	-
Ser138	x	x		x	x	x	-
Glu181	-	-	x	-	-	-	-
Leu225	-	-		-	-	-	x
Leu207	-	-		-	-	-	-
Ile16	x	x	x	x	x	x	x
Gln15	x	x	x	x	x	x	x
Tyr222	x	x	x	x	x	x	x
Val175	x	-		-	-	-	-

vdW
H-C
H
π-stacking
Halogen (F)
π-Sulfur
π-Cation

TOXICITY PREDICTION

The six best triazoles with the highest antifungal activity predicted by the QSAR-2D and 3D models were subjected to a toxicity test using ProTox II (https://tox-new.charite.de/protox_II/index.php?site=home). This website analyzes features of the most common fragments and chemical similarities to predict different toxicity parameters. These computerized toxicity predictions are helpful because they lessen the need for animal testing. These compounds were also subjected to quantitative estimation of similarity to fungicidal compounds (QEF), as proposed by Avram and colleagues [68].

This method is based on six pertinent descriptors that are likewise utilized in Lipinski's rule of five but have different values in this context as guidelines for producing a fungicide that can be predicted accurately. Thus, the molecular weight (MW), hydrophobicity (LogP), number of donors and acceptors of hydrogen bonds (HBD), number of rotatable bonds (RB), and number of aromatic bonds (arR) were employed for study.

To support these new compounds, these data were obtained from the Swiss ADME service (http://www.swissadme.ch/). The results are presented in Annex IX on supplementary material. **Compound 15** is particularly remarkable because it did not exhibit any toxicity throughout the toxicity testing of the ProTox II server.

Both triazoles are classify as rated 4 for toxicity, and neither of these candidates violates Lipinski's rule of five, which is an excellent result because it allows us to predict the oral bioavailability profile of new molecules [69]. As *Fusarium graminearum* is the main target of triazoles, these compounds should not, nevertheless, have a high bioavailability for humans, particularly for the compounds that demonstrated a likelihood of ≥ 50% liver toxicity, carcinogenicity and mutagenicity. To ensure the safety of these drugs, *in vitro* testing should be conducted even though QSAR models anticipate excellent biological activity against *F. graminearum*.

An analysis was subsequently conducted using the "QEPest" tool, which computes data for three classes of pesticides, to quantitatively evaluate the fungicidal effect of a specific molecule. The input data for each triazole are displayed in Table S20 on annex IX on supporting information, and the prediction outcomes are shown in **Table 5.** Using this information, the program predicted the three classes of pesticides: herbicides (QEH), insecticides (QEI) and fungicides (QEF). The values for finding a new compound were ≥ 0.72 for herbicides. ≥ 0.57 for insecticides and ≥ 0.6 for fungicides.

Table 5. Final results of compound prediction for the three classes: herbicide (QEH). Insecticide (QEI) and fungicide (QEF).

Compound	QEH	QEI	QEF
15	0.7032	0.5705	0.6025
20	0.3782	0.0	0.2128
21	0.4421	0.0	0.2865
22	0.4452	0.0	0.2819
25	0.3829	0.0	0.2171
27	0.3855	0.0	0.267
Carbendazim	0.4749	0.3549	0.4401

For many years, carbendazim was the most commonly used fungicide for treating *Fusarium*, but the QEPest experiment revealed that triazole **15** had more satisfactory

outcomes. Carbendazim has been produced and used extensively for several decades despite being thought to be hazardous and mutagenic to humans, as indicated by the ProTox II server. As numerous studies have already noted, carbendazim is more likely to pose a threat to human health in this scenario, even though its toxicity prediction is ranked as 6. As a result, its marketing has been halted in certain nations, including Brazil.

Molecular Dynamic (MD) Simulations

MD simulations were used to assess the interaction mechanism and stability of beta tubulin protein with the triazole derivative **15** and the commercial fungicide carbendazim, using the crystallographic ligand G2P as a control for the protein 7ZCW. Evaluations were done on the RMSD, RMSF, SASA, Rg, hydrogen bond analysis, and their affinities for binding with MM/GBSA.

Figure 8 shows that there was stability of the protein in all the complexes from 100 ns. The stability of the protein was also verified by analyzing the Solvent Accessible Surface Area (SASA) and the Radius of gyration (Rg), illustrated in figure S3 in annex VII on supplementary material, respectively. The SASA analyzes the exposure of the protein-receptor of the simulated complexes and determines how much the protein has been exposed to the solvent. With the turning radius (Rg), it is possible to calculate the structural compaction of the systems along the trajectory, in order to determine whether the complexes are folded or unfolded in a stable way [69].

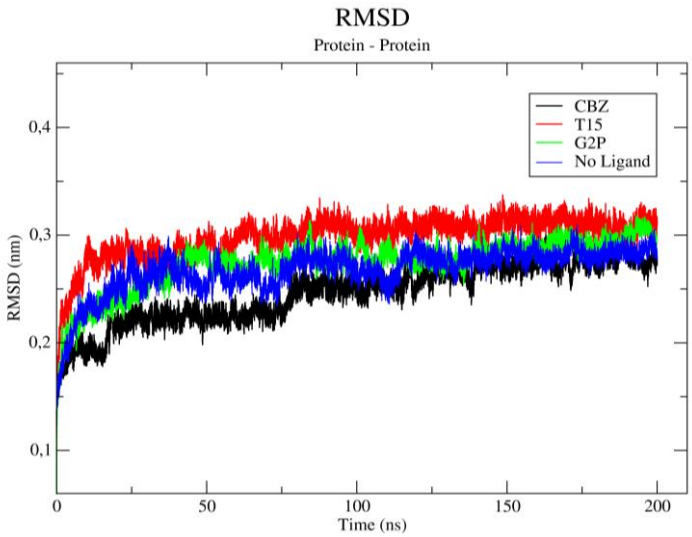

Fig. 8. Refers to the RMSD analysis of the protein in relation to the protein of the CBZ, T15 and G2P complexes over 200 ns of simulation.

We computed residual flexibility as RMSF (root mean square fluctuation) in order to establish a stronger connection between protein flexibility and the binding of these ligands. Higher stability is indicated by results with lower RMSF values, which are associated with residues in the protein's beta sheet and alpha helix regions. Higher values, on the other hand, suggest that the residues have varied more and are typically located in loop regions [70]. Accordingly, as **Figure 9** illustrates, the measurements showed some differences in the protein's backbone, pointing to the presence of specific peaks with larger variations that perfectly corresponded to the regions of residues 39–43, 276-280, 400–405, and 426. These are loop areas, according on a crystallographic structure analysis.

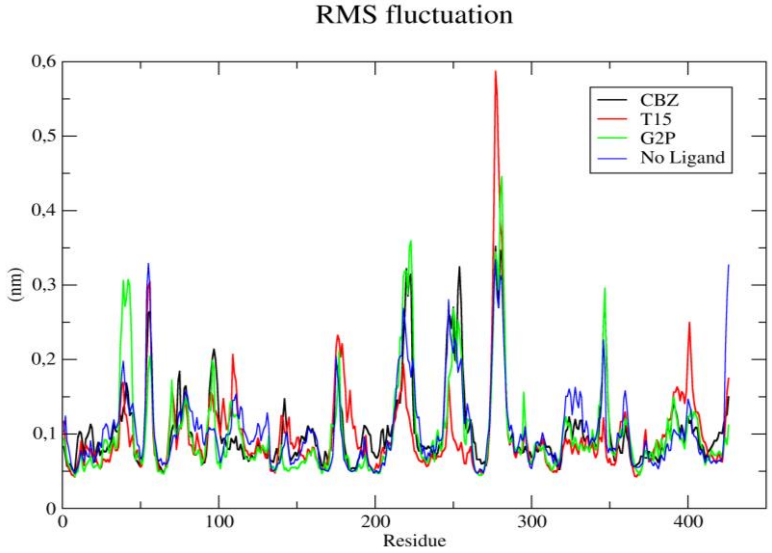

Fig. 9. RMSF analysis of the CBZ, T15, G2P and white complexes after a 200 ns molecular dynamics trajectory.

The active site of the protein is characterized by residues 8-16, 67-69, 72, 96-101, 104, 136-148, 167-172, 175-178, 181, 185, 204-205, 207-208, 221-226 and 229. To assess the fluctuations of these regions, we zoomed in on each band of the RMSF graph, which can be seen in Figure S1 (Annex VII of the supplemental material). In summary, T15 stabilized the protein in the following locations by interacting more with residues 8–16, 72, 96–101, 167–168, 204–208, and 221-229. Alternatively, CBZ was more active in regions 67–69, 72, 102–104, 138–139, 145–148, and 175–185.

The hydrogen bonds for each system during the simulation are displayed in Figure S2 in Annex VII of the supplemental material. As seen in the molecular docking, the G2P ligand has the most H-bonds overall. The fact that the molecule is substantially bigger than the others and has a phosphate group-rich end is one reason for this. In contrast, the CBZ ligand included more hydrogen bonds than T15. Despite the fact that CBZ and T15 only have one H-bond with the amino acid Asn226 according to the docking reports, it is still feasible to observe how the complex's behavior can be altered by the physiological environment as a result of dynamics. This may be explained by the fact that CBZ was the single ligand to leave the original location and go throughout the protein.

Estimating the free energy of interaction is crucial to understanding the ligands' interactions. With the support of the program gmx_MMPBSA v1.6.1 [71, 72], the binding affinity of the ligands could be determined and depicted in **Figure 10** using the MM/GBSA approach.

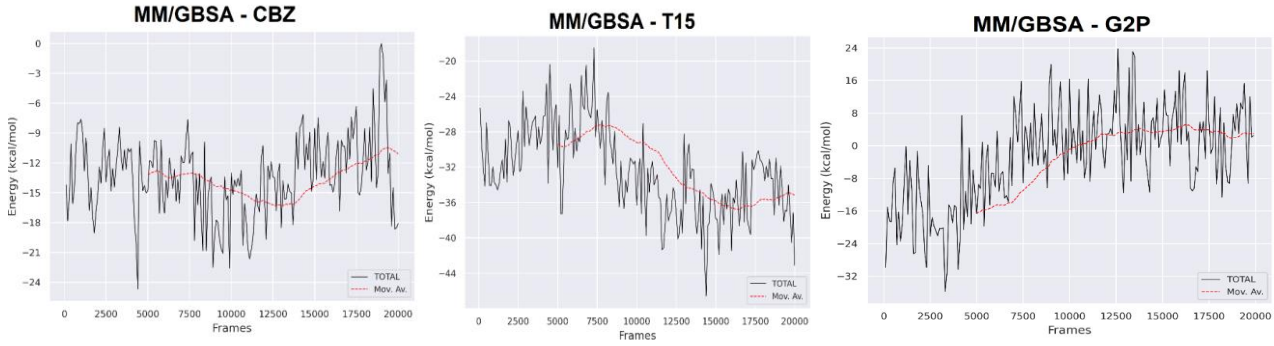

Fig. 10. MM/GBSA energy graph for carbendazim, triazole 15 and G2P, respectively.

A few frames that may have affected the energy peaks were examined. The CBZ, T15, and G2P are shown in **Figures 11** A, B, and C, respectively, at various points in time. It is evident that the CBZ envelops the protein and then moves behind it starting at 188 ns. The energy profile shows an abrupt peak change at 175 ns, with a spike to 0 kcal/mol after it was initially at -15 kcal/mol. The CBZ finds a new location about 190 ns and stays steady at -18 kcal/mol. In an effort to achieve stability, T15 slightly modifies its conformation at the beginning of the simulation. It eventually fits in more at position 3 (140 ns forward) and keeps this conformation until it reaches its minimal energy. This is seen in the MM/GBSA graph, where the smallest peak appears just before 150 ns. T15 then stabilizes at -44 kcal/mol at the end, retaining a conformation that is remarkably similar to the one that came before it. On the other hand, G2P, initially docked, undergoes a rearrangement in a new position and maintains this conformation until the end of the simulation.

3. Material and Methods

Building of QSAR models

To generate QSAR-2D and 3D models, a set of 27 quinazolin-4(3H)-one derivative molecules was employed, and their correspondingly antifungal activities against *Fusarium graminearum* were taked from Wang and coworkers [16], as illustrated in **Table 6**. Following a charge assessment at physiological pH 7.4, all of the molecules were drawn in MarvinSketch 12.94 and had a total charge of zero. Molecular descriptors were utilized as independent variables, while the *in vitro* inhibitory concentrations (or EC_{50} values; μmol/mL) of the substances were transformed into corresponding negative logarithms (pEC_{50} values), as dependent variables.

Using the Sybyl-X program, the alignment was completed based on compound **25**, which was the most active. The PM7 [20], RM1 [20], AM1-BCC [21], Gasteiger-Hückel [22], Gasteiger-Marsili [22, 23], MMFF94 [24], HF 3-21G [25], HF 6-311G [26], DFT 6-311G (B3LYP) [27] and RESP HF 6-311G [28] methods were used to compute the atomic partial charges of the molecules after alignment. The aim was to choose the model that best fit the different types of atomic partial charges.

Division into training and testing groups

The PaDEL Descriptor v2.21 program was used to first compute the fragment count and topological and geometric descriptors to ensure proper separation.

All descriptors that had a variance of 0.1 or less were initially removed from the model because they could not be used to categorize structures. In the second stage, all the remaining descriptors were evaluated for high correlation between them; i.e., when a pair of descriptors had a high correlation between them, one of them was excluded to avoid possible overfitting [29].

Using the clustering process carried out by the k-medoid algorithm, the remaining descriptors were fed into the k-medoid Clustering GUI 1.1 program (https://dtclab.webs.com/software-tools) to divide the compounds into training (19) and test (8) sets. This division ensured that the biological activity and the diversity of structures, molecules, and chemicals were preserved. A statistical model was not generated using the substances in the test group [30].

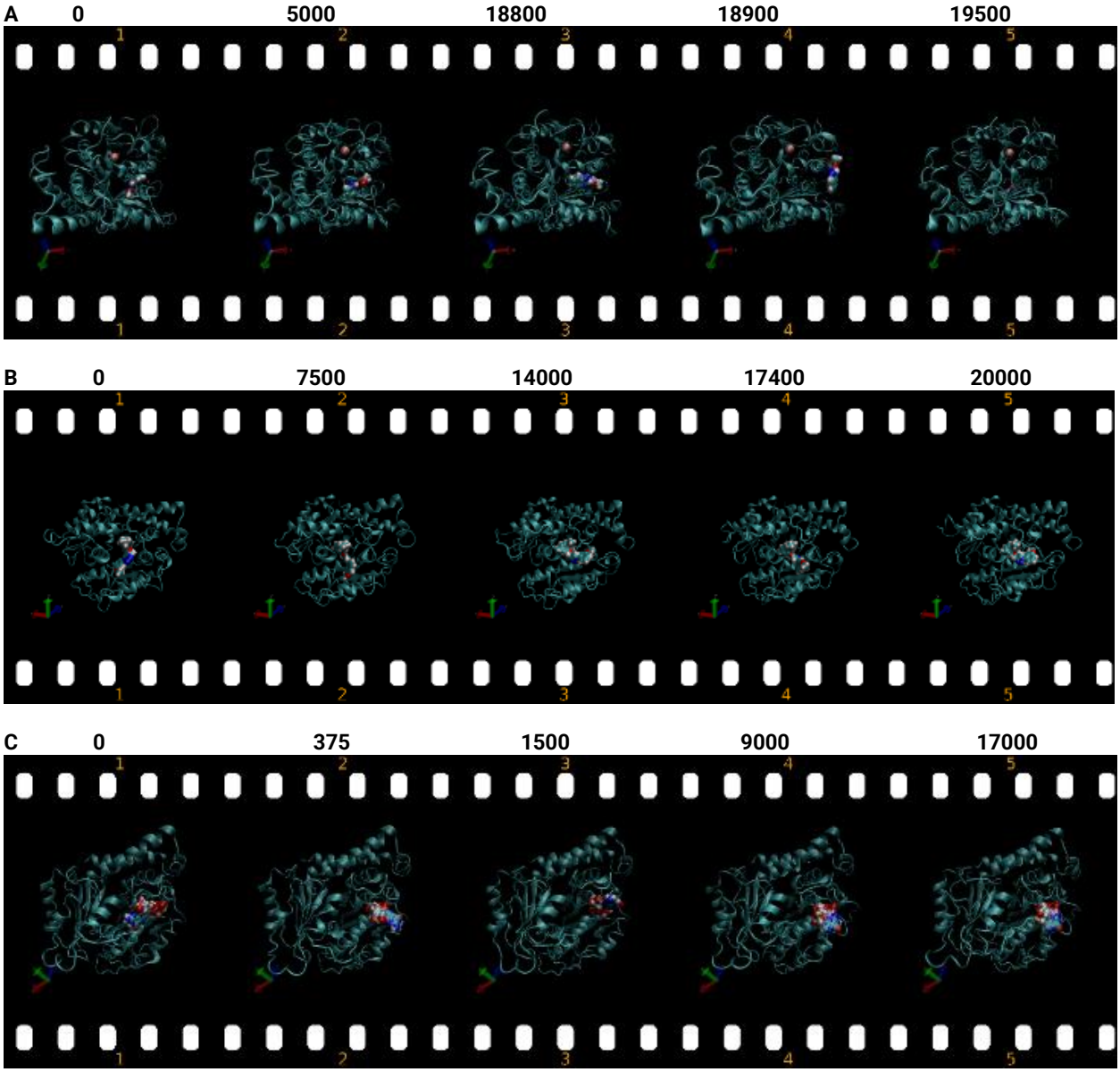

Fig. 11. A: CBZ in 0, 5000, 18800, 18900 and 19500 frames. B: 0, 7500, 14000, 17400, 20000 frames. C: 0, 375, 1500, 9000 and 17000 frames.

Table 6 - All the structures used in the training and test sets are listed, and their pEC_{50} values were calculated as $mol.L^{-1}$. Compound 25 was the most active between all them, and for this purpose, it was used as a model for aligning all the compounds by distill rigid generated by Sybyl-X.

TRAINING SET		
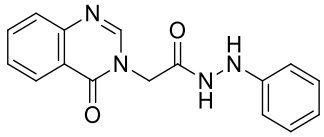	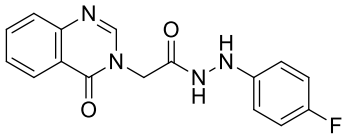	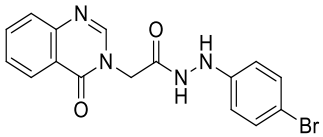
1 – pEC_{50}: 3.9485	2 – pEC_{50}: 5.3139	4 – pEC_{50}: 5.1005
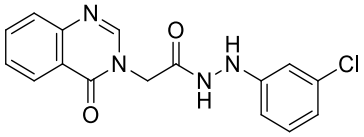	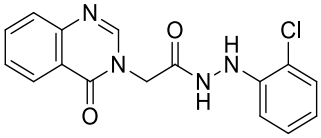	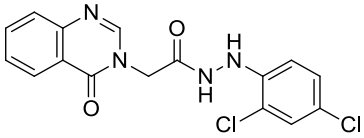
6 – pEC_{50}: 4.0962	7 – pEC_{50}: 3.1027	8 – pEC_{50}: 3.0488

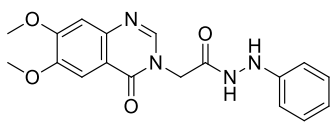

11 – pEC$_{50}$: 4.1858

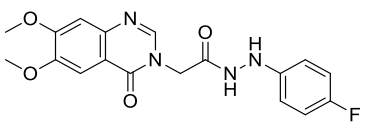

12 – pEC$_{50}$: 5.2601

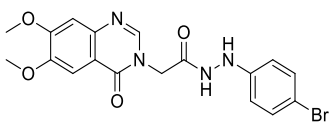

14 – pEC$_{50}$: 5.1494

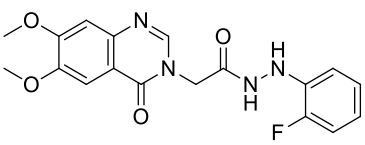

15 – pEC$_{50}$: 3.4659

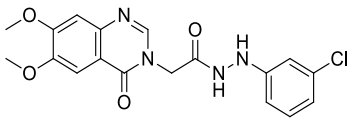

16 – pEC$_{50}$: 4.2947

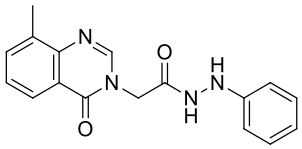

18 – pEC$_{50}$: 4.1391

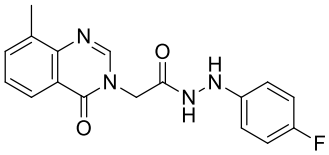

19 – pEC$_{50}$: 5.2894

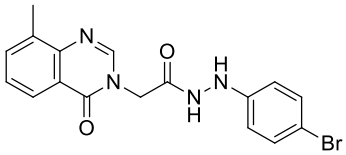

21 – pEC$_{50}$: 4.9635

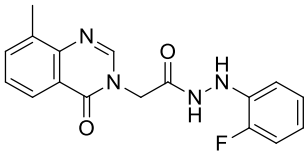

22 – pEC$_{50}$: 3.8510

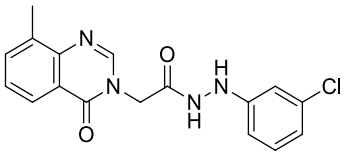

23 – pEC$_{50}$: 4.4228

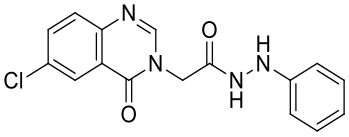

24 – pEC$_{50}$: 4.2894

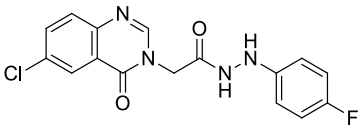

25 – pEC$_{50}$: 5.4505

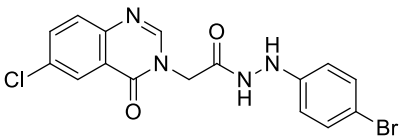

27 – pEC$_{50}$: 5.1383

TEST SET

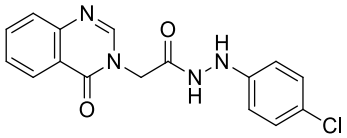

3 – pEC$_{50}$: 5.2718

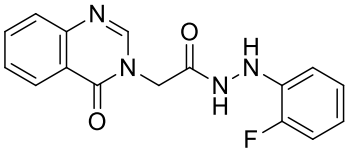

5 – pEC$_{50}$: 3.2950

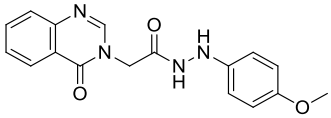

9 – pEC$_{50}$:.2938

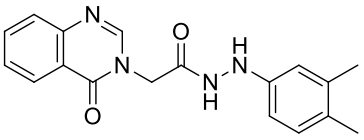

10 – pEC$_{50}$: 4.2263

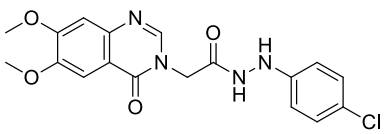

13 – pEC$_{50}$: 5.1619

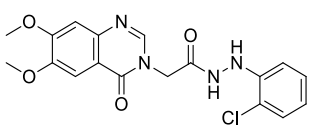

17 – pEC$_{50}$: 3.1901

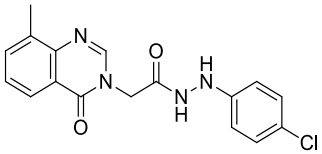

20 – pEC$_{50}$: 5.1462

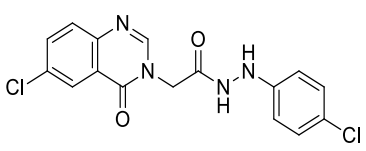

26 – pEC$_{50}$: 5.2611

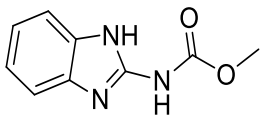

Carbendazim* – pEC$_{50}$: 5.6380

*Carbendazim was not part of the training and test division but was subsequently used as a test for activity prediction.

QSAR-2D

The QSAR-2D model was produced by inputting the descriptors from the training and test separation into the Best Subset Selection v2.1 algorithm (**https://sites.google.com/site/dtclabmlrbss/**), which analyses every conceivable combination of descriptors. The

Jamovi v2.3 (2022) program was used to conduct a thorough analysis of the best statistical models that were produced. When using descriptors, statistical processing is essential for enhancing their prediction power. Thus, following linear regression, each model's Durbin–Watson autocorrelation test (DW < 2), variance inflation factor (VIF < 5), Shapiro–Wilk normality test ($p > 0.05$), R, and modified R^2 (> 0.6) were computed to verify the assumptions. Finally, biological activity was predicted using the best-found equation.

QSAR-3D

Following molecular alignment and partial atomic charge calculations, QSAR-3D CoMFA and CoMSIA models were produced using the training set's molecular field interactions (MIFs). The QSAR module found in Sybyl-X (v2.1.,Tripos, Inc., St. Louis, MO, USA) was used to conduct these studies.

The compounds were placed into a grid, or three-dimensional box, and assigned a minimum distance between 0.5 to 2 Å the box's edges and the aligned compounds. Like a sp^3 carbon and with a +1 charge, a molecular probe from the SYBYL-X 2.1.1 program passes across each grid intersection point, producing numerical values in each quadrant. Variations in the model's coefficient weights and grid distance are encouraged by a procedure known as focusing. The chosen focus (0.5, 1.0, or 1.5 Å) determines the reading variation distance (d). The three focuses were utilized to create a thorough scan of the molecule to enhance the creation of the 3D models. We not only changed the grid spacing but also multiplied the weights by the model regression coefficient (w) variation of each point. These weights ranged from 0.3 to 0.9, as previously published by De Paula and coworkers [31]. This can be compared to the image enhancement of the CoMFA and CoMSIA models.

A PLS analysis was performed during the first validation phase to determine the relationship between the biological activity levels (pEC_{50}) and the CoMFA molecular fields. The model was then cross-validated using the leave-one-out (LOO) technique. At this point, Sybyl provides the ideal number of components in addition to the cross-validation prediction's (SEP), q^2 and standard error. The final step involved repeating the PLS analysis using the optimal number of components that were previously acquired to calculate the standard error of the estimate (SEE) and the correlation coefficient (r^2).

To create multivariate statistical models in CoMSIA, the models were also assessed using the partial least squares (PLS) method. The results such as the correlation coefficient (r^2), cross-validation coefficient (q^2), and their corresponding errors (SEE and SEP) are given using the leave-one-out methodology [32].

COMPARATIVE MODELING

A comparative modeling methodology was used to identify a protein that resembles the β-tubulin protein of *F. graminearum*, which is currently absent from the Protein Data Bank (PDB) database. Originally, the National Center for Biotechnology Information (NCBI) provided the primary sequence of the β-tubulin protein of the fungus *F. graminearum* **Q4HZS8.1**. To locate a potential model, three servers and software were utilized. Swiss Model, Phyre2, and Alphafold were used as the servers. Modeler was the program used. The Procheck [33] and Verify3D [34] servers (https://saves.mbi.ucla.edu/) were used to verify the quality of the templates created; the microtubule complex of *Homo sapiens* (PDB:7ZCW) was the best template selected.

DOCKING MOLECULAR

Using the GOLD 2022.3.0 program (CCDC Software Ltd., Cambridge, UK), the crystallographic ligand between the human tubulin protein's α and β chains (PDB: 7ZCW) was first redocked. Using the four scoring functions, Chemscore, ASP, GoldScore, and ChemPLP, which assess and score various ligand conformations with respect to the protein binding site, the redocking approach was executed at cavity diameters of 5 Å, 7 Å, and 10 Å around the ligand. The best conformation of the ligand was then selected and analyzed by PyMOL v.2.5.2 [35], and the interactions were highlighted by Discovery Studio Visualizer [36].

Following the redocking stage, the optimal configuration was determined for use in molecular docking. The quantity of interactions corresponding to the crystallographic ligand and the position of the ligand were used to determine which postures were optimal.

MOLECULAR DYNAMICS SIMULATION

Firstly, only the B monomer and its G2P ligand were included in the crystallographic protein found in the PDB (7ZCW). PyMOL software was used to extract both. By employing the Marvin Sketch program to examine the ligand's charges, a formal charge of -3 at physiological pH was found. The ligand needs to be parameterized using two programs: Mktop [37], which creates the ligand's '.top' output file; and Acpype [38] (using the keywords: acpype -i ligand.pdb -n -3), which will ultimately generate the '.gro' and '.itp' output files. The reason this parameterization matters is due to the fact it prepares the ligand for use as an input in molecular dynamics, which was done with the computational software GROMACS 2016.4 (http://www.gromacs.org). Since OPLS/AA (Optimized Potentials for Liquid Simulations All Atoms) is targeted at organic molecules and biomolecular systems, it was selected as the force field [39].

The PropKa server [40] (**https://www.ddl.unimi.it/vegaol/propka.htm**) was used to determine the protonation state of the protein's amino acids. It calculates the pKa of amino acid residues at physiological pH 7.4. At this point, the amino acids Cys, Tyr, Lys, and Arg were protonated, and the protein had a formal charge of -15. In order to neutralize the overall charge, sodium ions had to be added to the system as counter-ions to balance the charges. TIP3P-type water molecules were contained in a cubic box with the system (protein, ligand, and Mg) positioned inside at a distance of 1.5 nm [41].

Energy minimization was carried out using the maximum slope method (by the Steepest Descent algorithm), which seeks to find the local minimum of the potential energy surface by making adjustments to the positions of the molecule's atoms. This initial optimization of the system was carried out in up to 20,000 steps. Additionally, this approach seeks to remove any inaccurate initial structures that may have been introduced during system formation and could have resulted in a simulation failure.[42] The Newton–Raphson approach, which employs both first-order and second-order derivatives to identify an ideal search direction and apply the necessary parameter adjustments, was subsequently used to minimize the system [43].

To accommodate the water molecules in the system, the improved protein–ligand complex was initially subjected to 500 ps of molecular dynamics at 310 K. This process involved restricting the position of the β-tubulin atoms connected to G2P. After this, at 100 ns, molecular dynamics were performed without position constraints at 310 K and 1 bar of

pressure, with a cutoff radius of 10 Å for van der Waals and electrostatic interactions and an integration time interval of 2 fs (0.002 ps). Using a Berendsen barostat, this stage was conducted with a constant set of particle number, pressure, and temperature (NPT) [44]. To preserve the integrity of the molecules and enable a more stable and realistic representation during the molecular dynamics simulation, the Particle Mesh Ewald (PME) algorithm [45] was utilized to calculate the electrostatic interactions, and the LINCS algorithm [46] was used to constrain the bonds between the atoms.

TRIAZOLE-DERIVATIVE NATURAL PRODUCTS SCREENING

After the QSAR models were constructed, the next step was to apply them to predict the antifungal activity of our study group's library of compounds produced from triazole derivatives from thymol [17], flavonone [18] and isatin derivatives [19]. MarvinSketch 12.94 was used to construct the 32 compounds, which were then optimized, and their charges were assessed at physiological pH. Compounds 5, 19, and 25 had formal charges of -1, whereas the other compounds had formal charges of zero. These structures can be seen in Annex VI in supplemental information.

As previously reported, the optimal model equation for these novel triazole-derived compounds was utilized in QSAR-2D.

For the CoMFA and CoMSIA (QSAR-3D) models, the compounds were aligned based on the docking method [47]. The protein and crystallographic ligand (PDB ID: 7ZCW) served as inputs for the Gold 2022.3.0 software. Using the same score function validated by the redocking method, it was possible to find different poses and select only those that contained the triazole ring superimposed on the crystallographic ligand and the most active quinazoline derivative compound (**25**) for use in building the QSAR models. Subsequently, the partial atomic charges were calculated using the same method used to determine the best model. The probes were subsequently inserted into Sybyl-X, and the same procedure was carried out on the basis of the best focus of the model.

4. Conclusions

The ProTox II server's prediction does not pose any dangers to human health to compound **15**, that demonstrated enough data to qualify as a potent fungicide (QEF = 0.6025). This makes compound **15** an outstanding choice for controlling the fungus that causes fusariosis. This thymol-derived triazole also demonstrated insecticidal activity (QEI = 0.5705). Note that the CoMFA model (QSAR-3D) indicated that this compound had good predicted antifungal activity with a pEC_{50} = 4.727 $mol.L^{-1}$ was observed for *F. graminearum*.

The results of molecular dynamic simulations indicate the stability of the protein throughout the simulation, corroborated by the RMSD, SASA and Rg analyses. In terms of binding affinity, the triazole derived from thymol (15) showed more interactions in the active site regions, even though carbendazim showed more in the hydrogen bond interactions. On the other hand, in terms of energy, **T15** had a more effective interaction with the β-tubulin protein compared to the commercial fungicide carbendazim. The MM/GBSA results revealed a 2.4-fold higher energy for the triazole compared to carbendazim.

Thus, it is plausible to conclude that a promising molecule was found by building these models. We propose that this triazole molecule be used in *F. graminearum in vitro* tests for future study, in order to experimentally confirm the biological activity suggested by the *in-silico* analysis presented here.

Supporting Information

Supplementary material.

Acknowledgments

This study was made possible thanks to the resources provided by Coordenação de Aperfeiçoamento de Pessoal de Nível Superior - Brasil (CAPES).

Author Contributions

Larissa de Souza Gasques – Investigation, Methodology, Data curation, Project administration, Writing – original draft, Writing – review & editing. Pedro Alves Bezerra Morais – Funding acquisition, Resources.Arlan da Silva Gonçalves – Data curation, Software, Validation, Writing – review & editing. Heberth de Paula – Data curation, Methodology, Software, Validation, Writing – review & editing.

References and Notes

[1] Ducatti, R. D. B. Carragena como eliciadora em trigo e sua ação na biossíntese de desoxinivalenol por *Fusarium graminearum*. Dissertação [Master's thesis] – Pato Branco, Paraná, Brazil: Universidade Tecnológica Federal do Paraná, 2021. [Link]

[2] Wegulo, S. N.; Baenziger, P. S.; Nopsa, J. H.; Bockus, W. W.; Hallen- Adams, H. *Crop Protection* **2015**, *73*, 100. [Crossref]

[3] Powell, A. L.; Vujanovic, V. *Appl. Sci.* **2021**, *11*, 8960. [Crossref]

[4] Johns, L. E.; Bebber, D. P.; Gurr, S. J.; Brown, N. A. *Nature Food* **2022**, *3*, 1014. [Crossref]

[5] Calori-Domingues, M. A.; Almeida, R. R.; Tomiwaka, M. M.; Gallo, C. R.; Gloria, E. M.; Dias, C. T. S. *Food Sci. Technol.* **2007,** *27*, 181. [Crossref]

[6] Available from: https://www.apsnet.org/edcenter/disandpath/fungalasco/pdlessons/Pages/Fusariumport.aspx. Access April 2023.

[7] Yang, Y.; Li, M. X.; Duan, Y. B.; Li, T.; Shi, Y. Y.; Zhao, D.L; Zhou, Z. H.; Xin, W. J.; Wu, J.; Pan, X. Y.; Li, Y. J.; Zhu, Y. Y.; Zhou, M. G. *Pestic. Biochem. Physiol.* **2018**, *145*, 15. [Crossref]

[8] Santra, H. K.; Banerjee, D. In: Natural Bioactive Products in Sustainable Agriculture (Eds. J. Singh, A. Yadav). Springer, Singapore, 2020. p. 131-219. [Crossref]

[9] Augostine, C. R.; Avery, S. V. *Front. Microbiol*. **2022**, *13*, 866840. [Crossref]

[10] Kingston, D. G. I. *J Nat Prod*. **2011**, *74*, 5, 1352. [Crossref]

[11] Zhang, C. W.; Zhong, X. J.; Zhao, Y. S.; Rajoka, M. S. R.; Hashmi, M. H; Zhai, P.; Song, X. *Pharmacological Research - Modern Chinese Medicine* **2023**, *7*, 100262.

[Crossref]

[12] Cob-Calan, N. N.; Chi-Uluac, L. A.; Ortiz-Chi, F.; Cerqueda-García, D.; Navarrete-Vázquez, G.; Ruiz-Sánchez, E.; Hernández-Núñez, E. *Molecules* **2019**, *24*, 3387. [Crossref]

[13] Coutinho, C. F. B.; Galli, A.; Mazo, L. H.; Machado, S. A. S. Pesticidas: Revista de *Ecotoxicologia e Meio Ambiente*, **2006**, *16*, 63. [Crossref]

[14] Das, N. R.; Bera, K.; Sharma, T.; Toropova, A.; Toropov, A. A.; Achary, P. G. *J. Indian Chem. Soc.* **2022**, *99*, 100687. [Crossref]

[15] Zięba, A.; Laitinen, T.; Patel, J. Z.; Poso, A.; Kaczor, A. A. *Int. J. Mol. Sci.* **2021**, *22,* 6108. [Crossref]

[16] Wang, A.; Yang, Y.; Jun, Y.; Wang, B.; Lv, K.; Wang, H.; Liu, M.; Guo, H.; Lu, Y. *Bioorg. Med. Chem.* **2018**, *26,* 2073. [Crossref]

[17] Eloy, M. A.; Ribeiro, R.; Meireles, L. M.; Cutrim, T. A. S.; Francisco, C. S.; Javarini, C. L.; Borges, W.; Costa, A. V.; De Queiroz, V.; Scherer, R.; Júnior, V. L.; Morais, P. A. B. *J. Agric. Food Chem.* **2021**, *69*, 6958. [Crossref]

[18] Ribeiro, R.; Eloy, M. A.; Francisco, C. S.; Javarini, C. L.; Ayusso, G. M.; Fonseca, V. R.; Romao, W.; Regasini, L. O.; Araujo, S. C.; Almeida, M. O.; Honorio, K. M.; Paula, H.; Lacerda, Jr. V.; Morais, P. A. B. *Curr. Top. Med. Chem.* **2021**, *21*, 1999. [Crossref]

[19] Britto, K.; Francisco, C.; Ferreira, D.; Borges, B.; Conti, R.; Profeti, D.; Rodrigues, L.; Lacerda, V.; Morais, P. A. B.; Borges, W. *J. Braz. Chem. Soc.* **2019**, *31*, 476. [Crossref]

[20] Stewart, J. J. *J. Mol. Model.* **2013**, *19*, 1. [Crossref]

[21] Jakalian, A.; Jack, D. B.; Bayly, C. I. *J. Comput. Chem*. **2002**, *23,* 1623. [Crossref]

[22] Gasteiger, J.; Marsili, M. *Tetrahedron* **1980**, *36*, 3219. [Crossref]

[23] Gasteiger, J.; Marsili, M. *Organ. Magn. Reson*. **1981**, *15*, 353. [Crossref]

[24] Halgren, T. A. MMFF VII. *J. Comput. Chem*. **1999**, *20,* 730. [Crossref]

[25] Stephen, B. J.; Pople, J. A.; Hehre, W. J. *J. Am. Chem. Soc*. **1980**, *102*, 939. [Crossref]

[26] Krishnan, R.; Binkley, J. S.; Seeger, R.; Pople, J. A. *J. Chem. Phys*. **1980**, *72*, 650. [Crossref]

[27] Stephens, P. J.; Devlin, F. J.; Chabalowski, C. F.; Frisch, M. J. *J. Phys. Chem.* **1994**, *98*, 11623. [Crossref]

[28] Madhavan, T.; Gadhe, C. G.; Kothandan, G.; Lee, K.; Cho, S. J. *Int. J. Quantum Chem.* **2011**, *112*, 995. [Crossref]

[29] Mascarenhas, R. M. G.; Lima, C. A.; Rodrigues, R. P.; Kitagawa, R. R.; Faraoni, A. S.; Oliveira, T. B.; Kitagawa, R. R.; Faraoni, A. S.; Oliveira, T. B. V. *Rev. Virtual Quim.* **2019**, *11,* 543. [Crossref]

[30] Alves, V. M.; Braga, R. C.; Muratov, E. N.; Andrade, C. H. *Quim. Nova* **2018**, *41*, 202. [Crossref]

[31] De Paula, H.; Angelo, R. M.; Honorio, K. M. *J. Mol. Model.* **2021**, *27*, 239. [Crossref]

[32] Vyas, V. K.; Ghate, M.; Gupta, N. *Arabian J. Chem.* **2017**, *10,* 2182. [Crossref]

[33] Laskowski, R. A.; MacArthur, M. W.; Moss, D. S.; Thornton, J. M. *J. Appl. Crystallogr.* **1993**, *26*, 283. [Crossref]

[34] Bowie, J. U.; Lüthy, R.; Eisenberg, D. *Science.* **1991,** *253,* 164. [Crossref]

[35] PyMOL. The PyMOL Molecular Graphics System, Version 2.5.2 Schrödinger, LLC.

[36] BIOVIA, D. S. Discovery Studio Visualizer. San Diego, 2019.

[37] Ribeiro, A. A.; Horta, B. A.; Alencastro, R. B. *J. Braz. Chem. Soc*. **2008**, *19*, 1433. [Crossref]

[38] Silva, A. W. S.; Vranken, W. F. *BMC Research Notes* **2012**, *5*, 367. [Crossref]

[39] Jorgensen, W. L.; Maxwell, D. S.; Tirado-Rives, J. *J. Am. Chem. Soc.* **1996**, *118*, 45, 11225. [Crossref]

[40] Li, H.; Robertson, A. D.; Jensen, J. H. *Proteins: Struct., Funct., Bioinf.* **2005**, *61,* 704. [Crossref]

[41] Dos Santos, M. A. F.; Habitzreuter, M. A.; Schwade, M. H.; Antonacci, M.; Gonzatti, G.K.; Netz, P. A.; Barbosa, M. C. *J. Chem. Phys.* **2019**, *150*, 235101. [Crossref]

[42] Abraham, M. J.; Murtola, T.; Schulz, R.; Pall, S.; Smith, J. C.; Hess, B.; Lindahl, E. *SoftwareX*. **2015**, *1*, 19. [Crossref]

[43] Namba, A. M.; Da Silva, V. B.; Da Silva, C. H. T. P. *Ecl. Quím.* **2008**, *33,* 13. [Crossref]

[44] Lin, Y.; Pan, D.; Li, J.; Zhang, L.; Shao, X. *J. Chem. Phys*. **2017**, *146*, 124108. [Crossref]

[45] Darden, T.; York, D.; Pedersen. L. *J. Chem. Phys.* **1993**, *98*, 10089. [Crossref]

[46] Hess, B.; Henk, B.; Berendsen, H. J. C.; Fraaije, J. G. E. M. *J. Comput. Chem.* **1998**. [Crossref]

[47] Zhang, X.; Mao, J.; Li, W.; Koike, K.; Wang, J. *Comput. Biol. Chem.* **2019**, *83*, 107134. [Crossref]

[48] Leemans, E.; Mahasenan, K. V.; Kumarasiri, M.; Spink, E.; Ding, D.; O'daniel, P. I.; Boudreau, M. A.; Lastochkin, E.; Testero, S. A.; Yamaguchi, T.; Lee, M.; Hesek, D.; Fisher, J. F.; Chang, M.; Mobashery, S. *Bioorg. Med. Chem. Lett.* **2016**, *26*, 1011. [Crossref]

[49] Chavda, J.; Bhatt, H. *Struct. Chem.* **2019**, *30*, 2093. [Crossref]

[50] Kumar, S. P.; Jha, P. C.; Jasrai, Y. T.; Pandya, H. A. *J. Biomol. Struct. Dyn.* **2016,** *34,* 540. [Crossref]

[51] Krishna, K. M.; Inturi, B.; Pujar, G. V.; Purohit, M. N.; Vijaykumar, G. S. *Eur. J. Med. Chem.* **2014**, *84*, 516. [Crossref]

[52] Walter, M. E.; Almeida, V. L.; Nunes, R. J. *Quim. Nova* **2013**, *36*, 691. [Crossref]

[53] El-Mernissi, R.; Khatabi, K. E.; Khaldan, A.; Elmchichi, L.; Shahinozzaman, M.; Ajana, M. A.; Lakhlifi, T.; Bouachrine, M. *J. Mex. Chem. Soc.* **2022**, 66. [Crossref]

[54] Nilewar, S. S.; Kathiravan, M. K. *J. Chemom.* **2014**, *28*, 60. [Crossref]

[55] Ashraf, N.; Asari, A.; Yousaf, N.; Ahmad, M.; Ahmed, M.; Faisal, A.; Saleem, M.; Muddassar. M. *Front. Chem*. **2022,** *10*, 1003816. [Crossref]

[56] Roman, D. L.; Voiculescu, D. I.; Filip, M.; Ostafe, V.; Isvoran, A. *Agriculture* ***2021****, 11,* 893. [Crossref]

[57] Wang, Y.; Ning, X.; Li, G.; Sang, N. *J. Hazard. Mater.* **2022**, *424*, 127479. [Crossref]

[58] Tarafder, M.; Datta, B. *Curr. Genet.* **2022***, 68*, 429. [Crossref]

[59] Ramirez-Rios, S.; Choi, S. R.; Sanyal, C.; Blum, T. B.; Bosc, C.; Krichen, F.; Denarier, E.; Soleilhac, J. M.; Blot, B.; Janke, C.; Stoppin-Mellet, V.; Magiera, M. M.; Arnal,

I.; Steinmetz, M. O.; Moutin, M. J. *J. Cell Biol*. **2023**, *222,* e202205096. [Crossref]

[60] Waterhouse, A.; Bertoni, M.; Bienert, S.; Studer, G.; Tauriello, G.; Gumienny, R.; Heer, F. T.; De Beer, T. A. P.; Rempfer, C.; Bordoli, L.; Lepore, R.; Schwede, T. *Nucleic Acids Res*. **2018**, *46,* 296. [Crossref]

[61] Bertoni, M.; Kiefer, F.; Biasini, M.; Bordoli, L.; Schwede, T. *Scientific Reports*. **2017**, *7*, 10480. [Crossref]

[62] Vela-Corcía, D.; Romero, D.; De Vicente, A.; Pérez-García, A. *Sci. Rep.* **2018**, *8*, 7161. [Crossref]

[63] Bindewald, E.; Skolnick, J. *J. Comput. Chem.* **2005**, *26,* 374. [Crossref]

[64] Laskowski, R. A.; Macarthur, M. W.; Moss, D. S.; Thornton, J. *J. Appl. Crystallogr.* **1993**, *26*, 283. [Crossref]

[65] Zhu, Y.; Liang, X.; Li, Y.; Duan, Y.; Zheng, Z.; Wang, J.; Zhou, M. *Phytopathology* **2018**, *108*, 352. [Crossref]

66] Islamiati, E. D.; Widada, J.; Wahyuningsih, T. D.; Widianto, D. *Agric. Nat. Resour.* **2022,** *56,* 899. [Crossref]

[67] Zhu, Y.; Liang, X.; Li, Y.; Duan, Y.; Zheng, Z.; Wang, J.; Zhou, M. *Phytopathology* **2018**, 108, 352. [Crossref]

[68] Avram, S.; Funar-Timofei, S.; Borota, A.; Chennamaneni, S. R.; Manchala, A. K.; Muresan, S. *J Cheminform*. **2014,** *6,* 42. [Crossref]

[69] Da Costa, R. A.; Da Rocha, J. A. P.; Pinheiro, A. S.; Da Costa, A. S. S.; Da Rocha, E. C. M.; Silva, R. C.; Gonçalves, A. S.; Santos, C. B. R.; Brasil, D. S. B. *Molecules* **2022**, *27*, 4118. [Crossref]

[70] Shahroz, M. M.; Sharma, H. K.; Altamimi, A. S. A.; Alamri, M. A.; Ali, A.; Ali, A.; Alqahtani, S.; Altharawi, A.; Alabbas, A. B.; Alossaimi, M. A.; Riadi, Y.; Firoz, A.; Afzal, O. *Molecules* **2022,** *27*, 1159. [Crossref]

[71] Valdés-Tresanco, M. S.; Valdés-Tresanco, M. E.; Valiente, P. A.; Moreno, E. *J. Chem. Theory Comput.* **2021**, *17*, 6281. [Crossref]

[72] Miller, B. R.; Mcgee, T. D.; Swails, J. M.; Homeyer, N.; Gohlke, H.; Roitberg, A. E. *J. Chem. Theory Comput.* **2012**, *8*, 3314-3321. [Crossref]

How to cite this article

Gasques, L. S.; Morais, P. A. B.; Gonçalves, A. S.; de Paula, H. *Orbital: Electronic J. Chem*. **2025**, *17*, 322. DOI: http://dx.doi.org/10.17807/orbital.v17i4.22921